We are IntechOpen,
the world's leading publisher of
Open Access books
Built by scientists, for scientists

6,900
Open access books available

186,000
International authors and editors

200M
Downloads

Our authors are among the

154
Countries delivered to

TOP 1%
most cited scientists

12.2%
Contributors from top 500 universities

CLARIVATE ANALYTICS
BOOK CITATION INDEX
INDEXED

WEB OF SCIENCE™

Selection of our books indexed in the Book Citation Index
in Web of Science™ Core Collection (BKCI)

Interested in publishing with us?
Contact book.department@intechopen.com

Numbers displayed above are based on latest data collected.
For more information visit www.intechopen.com

Fine Biomedical Imaging Using
X-Ray Phase-Sensitive Technique

Akio Yoneyama[1], Shigehito Yamada[2] and Tohoru Takeda[3]
[1]Advanced Research Laboratory, Hitachi Ltd.
[2]Congenital Anomaly Research Center, Kyoto University
[3]Allied Health Sciences, Kitasato University
Japan

1. Introduction

X-ray imaging is widely used for non-destructive observations of the inner structures of samples in many fields, such as biological, clinical, and industrial ones. The transparency of X-rays is much higher than that of visible light, and therefore the spatial distribution of X-ray intensity passing through a sample (radiography) can visualize the mass-density distribution inside the sample. However, X-ray intensity barely changes when passing through samples consisting of a light element, such as carbon, oxygen, or nitrogen, because of the extremely high transmittance of X-rays. Therefore, the sensitivity of absorption-contrast X-ray imaging is not sufficient for carrying out fine observations of samples such as biological soft tissues and organic materials. Contrast agents, including heavy elements such as iodine, and long exposure to X-rays are ordinarily used to improve sensitivity. However, these supplementary methods may cause allergic reactions and expose subjects to extremely high X-ray dosages.

A fundamental solution to this problem is use of the phase information of X-rays. X-rays are electromagnetic waves having very short wavelength and are mainly characterized by their amplitude and phase. When they pass through samples, their amplitude is decreased and the phase is shifted. In the hard X-ray region, the cross-section of phase shift for light elements is about 1000 times larger than that of absorption (Momose & Fukuda, 1995). Therefore, phase-contrast X-ray imaging, which uses phase shift caused by the sample as image contrast, provides a way of conducting fine observations of biomedical samples without the need for contrast agents or excessive X-ray dosages.

For phase-shift detection, it is essential to convert the phase shift into the change in X-ray intensity because we can only detect the intensity of X-rays by using current-detecting devices. Many conversion methods, such as interferometry with an X-ray crystal interferometer (Momose & Fukuda, 1995; Momose, 1995; Takeda et al., 1995), diffractometry with a perfect analyzer crystal (Davis et al., 1995; Ignal and Beliaevskaya, 1995; Chapman et al., 1997), a propagation-based method with a Fresnel pattern (Snigirev et al., 1995; Wilkins et al., 1996), and Talbot interferometry with a Talbot grating interferometer (Momose et al., 2003; Weitkamp et al., 2005), have been developed recently. The principle difference between these methods is in the detection of physical values; that is, interferometry detects the phase shift directly, while the other methods detect the first or second spatial derivation of the phase shift.

Therefore, interferometry has the highest sensitivity and is suitable for radiographic and three-dimensional (3D) observation of samples requiring high density resolution, such as biomedical soft tissues. On the other hand, the other methods have a large dynamic range of density and are suitable for observation of samples including regions with large differences in density, such as bone and soft tissues (Yoneyama et al., 2008).

Among these methods, interferometry and diffractometry are two major techniques for biomedical imaging, and 2D and 3D observations of various biomedical samples have been performed using synchrotron radiation. Note that Talbot interferometry using a conventional X-ray source has been studied actively for clinical use recently (Momose, 2009; Donath et al., 2010), because it has the advantage of cone-beam and/or polychromatic X-rays being useable.

Early X-ray interferometric imaging (XII) was achieved by using a monolithic crystal X-ray interferometer having three wafers cut from one silicon ingot (Bonse & Hart, 1965). Radiographic observations of rat cerebella (Momose & Fukuda, 1995), metastatic liver tumors in humans (Takeda et al., 1995), and cancerous breast tissues (Takeda et al., 2004) were conducted. The high sensitivity of XII enables differences in biological soft tissues such as cancers and normal tissues to be visualized. Phase-contrast X-ray computed tomography was also achieved in combination with general computed tomography (Momose et al., 1995). Non-destructive 3D observations of small columnar samples of various biological soft tissues were made (Momose et al., 1996; Takeda et al., 2000). To broaden the scope of interferometry to biomedical applications such as *in vivo* observations, imaging systems fitted with a two-crystal X-ray interferometer (Becker & Bonse, 1974) have been developed (Yoneyama et al., 1999, 2002, 2004a). The latest version of the system has a 60 × 40-mm field of view at an X-ray energy of 17.8 keV (Yoneyama et al., 2004a), and it enables 3D observations with a density resolution of less than 1 mg/mm^3. By using this system, *in vivo* radiographic observation of blood flow in a rat liver (Takeda et al., 2004a), *in vivo* 3D observation of a tumor implanted in nude mice (Takeda et al., 2004b; Yoneyama et al., 2006), and quantitative analysis of β-amyloid plaques in brains extracted from Alzheimer's disease model mice (Noda-Saita et al., 2006) were successfully performed.

Diffractometry was expanded and termed diffraction-enhanced imaging (DEI) for fine biomedical observations (Chapman et al., 1997). With this method, observations of breast cancer tissues (Pisano et al., 2000), articular cartilage (Mollenhauer et al., 2002; Ando et al., 2004), and amyloid plaques in the brain of a mouse model of Alzheimer's disease (Connor et al., 2009) were performed. The results showed that DEI had a higher sensitivity than that of conventional radiography and computed tomography. In addition, many developments in DEI (recently known by the more generic name of analyzer-based imaging (ABI)) have also been actively studied, and three images of a sample depicting refraction, ultra-small-angle scatter, and absorption have been obtained recently (Oltulu et al., 2003; Wernick et al., 2003; Rigon et al., 2007). To shorten the measurement time and lower the X-ray dose, a new derivative method using two diffraction beams (forward and normal) was also developed, and a fine tomographic image of breast cancer was obtained (Sunaguchi et al., 2010). In addition, high-energy DEI was developed to extend the dynamic range of density, and an obtained image of an electrical cable showed clearly not only the core and ground wire made of copper but also the isolator and outer jacket made of polymer (Yoneyama et al., 2009).

In this chapter, we will describe the principle of phase-contrast X-ray imaging, two major methods for detecting X-ray phase-shift (XII and DEI), imaging systems for XII and DEI, and examples of fine 2D and 3D images of pathological soft tissues and mice embryos.

2. Principle, methods, and imaging system

2.1 Principle of phase-contrast imaging

When X-rays pass through a sample, their amplitude is decreased by absorption and their phase is shifted as shown in Fig. 1 (a). In the hard X-ray region, the refractive index n of the sample is written as

$$n = 1 - \delta - i\beta \tag{1}$$

$$\delta = \frac{\lambda^2 r_e}{2\pi} \sum_i N_i (Z_i + f'_i) \tag{2}$$

$$\beta = \frac{\lambda^2 r_e}{2\pi} \sum_i N_i f''_i, \tag{3}$$

where r_e is the classical electron radius, λ is the wavelength of the X-ray, N_i is the atomic density of element i, Z_i is the atomic number of element i, and f'_i and f''_i are the real and imaginary parts respectively of the anomalous scattering factor of element i. By using these constituents of the refractive index, the X-ray intensity change $\ln(I/I_\text{o})$, caused by amplitude decrease in a uniform-density sample, is given by

$$\ln\left(\frac{I}{I_o}\right) = -\frac{4\pi\beta t}{\lambda} \tag{4}$$

and the phase-shift $d\theta$ is given by

$$d\theta = \frac{2\pi\delta t}{\lambda}, \tag{5}$$

where t is the thickness of the sample. Conventional absorption-contrast X-ray imaging uses $\ln(I/I_\text{o})$ as image contrast while phase-contrast X-ray imaging uses $d\theta$. Therefore, the sensitivity ratio between absorption- and phase-contrast imaging is given by the ratio of β to δ. The calculated sensitivity ratios (δ/β) to atomic number for various X-ray energies are plotted in Fig. 1(b). The results show that the ratio of light elements, such as hydrogen, oxygen, nitrogen, and carbon, runs to about 1000 times. Thus, the sensitivity of phase-contrast X-ray
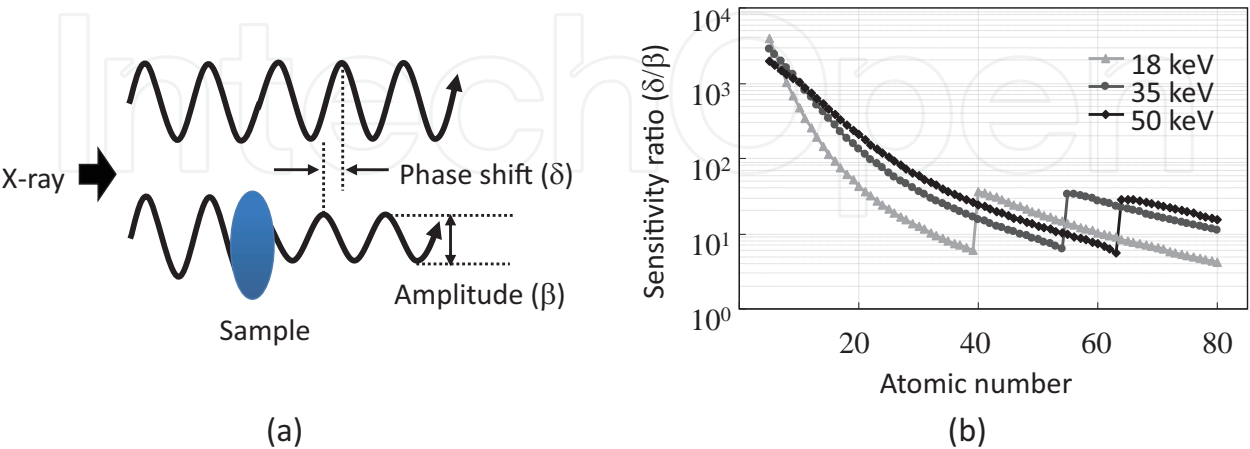

Fig. 1. (a) Interaction between X-ray and sample. When X-ray passes through sample, its amplitude is decreased and phase is shifted. (b) Sensitivity ratios between phase- and absorption-contrast imaging. Ratios increase to about 1000 for light elements.

imaging for light elements is about 1000 times higher than that of absorption-contrast X-ray imaging in principle. The high sensitivity of phase-contrast X-ray imaging provides many advantages for biomedical observations. First, fine observations of samples consisting of light elements, such as biological soft tissues and organic materials, can be performed in a short measurement time. Second, the usage of contrast agents is not required, and therefore the density distribution in a sample can be measured independently without considering reactions to contrast agents. Third, δ is almost proportional to the electron density of samples and the square of X-ray energy while β changes abruptly near the energy of the absorption edges; density distribution in a sample can be measured without considering the influence of the difference of the X-ray energy.

Conventional X-ray computed tomography (CT) uses intensity change $\ln(I/I_o)$ in samples as input data for reconstruction calculations. When X-rays pass through samples having different density and element regions, $\ln(I/I_o)$ is written as

$$\ln\left(\frac{I}{Io}\right) = \frac{4\pi}{\lambda} \int \beta \, dz, \tag{6}$$

where the integration is carried out along the direction of the X-rays. On the other hand, phase-shift $d\theta$ caused by the sample is written as

$$d\theta = \frac{2\pi}{\lambda} \int \delta dz. \tag{7}$$

The difference between the two equations above is only in δ and β, which are the same as in the radiographic observations. Therefore, CT using phase-shift information can be carried out using the same algorithm of reconstruction as conventional X-ray CT. The sensitivity of phase-contrast CT is about 1000 times higher than that of conventional CT for the same reason as previously mentioned for radiographic observation. In addition, $d\theta$ is proportional to the sample electron density; the obtained tomograms then provide the electron density distribution of the sample.

2.2 Phase-detection methods
2.2.1 Interferometric method

A schematic view of a monolithic triple Laue-case X-ray interferometer (Bonse & Hart, 1965) used in early X-ray interferometric imaging is shown in Fig. 2(a). This interferometer is made of silicon crystal and is monolithically cut from one silicon ingot to have three thin crystal wafers. The incident X-ray is divided into two beams (object and reference beams) at the first wafer (S), and these beams are reflected at the second wafer (M) by Laue-case X-ray diffraction. The reflected beams are then superposed at the third wafer (A), and they generate two interference beams by similar X-ray diffraction. Thus, this interferometer acts as a Mach-Zehnder interferometer in the visible light region. The intensity of the interference beams, I_i, is given by

$$I_i = I_o + I_r + 2\sqrt{I_0 I_r} v \cos(d\theta), \tag{8}$$

where I_o is the intensity of the object beam, I_r is that of the reference beam, v is the absolute value of the complex degree of coherence, and $d\theta$ is the phase shift caused by the sample placed in the path of the object beam. Therefore, $d\theta$ can be detected by measuring the interference intensity changes.

To obtain a quantitative phase map showing the spatial distribution of $d\theta$, a sub-fringe method, such as Fourier transfer (FT) (Takeda et al., 1982) and fringe scanning (FS) (Bruning et al., 1974), is required. The former method is traditionally used in *in vivo* observations as it is used to detect phase shifts from only one interference pattern. The latter method, which requires multiple interference images to calculate phase shift, has a wide dynamic range of density and high spatial resolution compared to that of FT. Therefore, this method is normally used for fine observations of static samples such as formalin-fixed biomedical soft tissues.

To broaden the scope of X-ray interferometric imaging in biomedical applications such as *in vivo* observations, a large-area field of view and suppression of the thermal disturbance caused by a sample's heat are indispensable. However, the monolithic X-ray interferometer cannot cope with these requirements because the field of view is limited by the size of the silicon ingot from which the interferometer was cut, and the sample cannot be set apart from the optical components of the interferometer due to the geometrical limitations. To overcome these limitations, a two-crystal X-ray interferometer consisting of two silicon-crystal blocks each having two crystal wafers has been developed (Fig. 2 (b)) (Becker & Bonse, 1974). By dividing the crystal block of the interferometer into two blocks, the field of view can be extended by four times or more. In addition, the distance between the crystal blocks and the sample can be kept long; the thermal influence, such as deformation of the crystal wafers caused by the sample's heat, is negligible and can be applied for the observation of living samples. On the other hand, a relative rotation between the blocks changes the X-ray phase very sensitively, and therefore rotational stabilization of the subnano-radian order is necessary for performing fine observations.
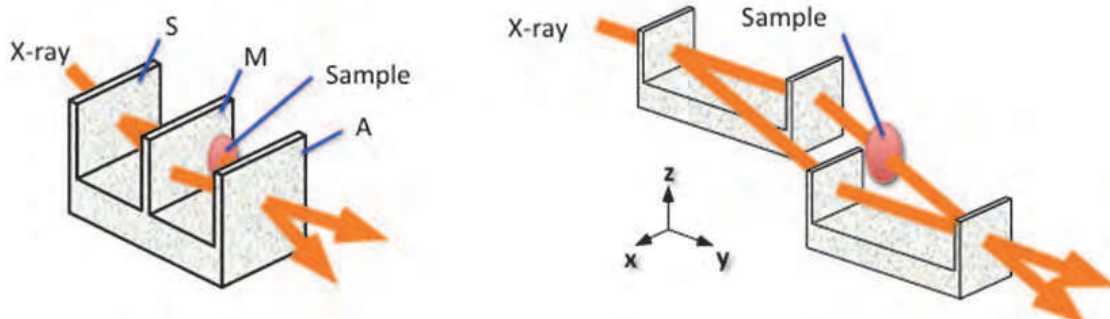

Fig. 2. (a) Monolithic triple Laue-case X-ray interferometer and (b) skew-symmetric two-crystal X-ray interferometer.

2.2.2 Diffraction-enhanced method

When X-rays pass through a sample, their optical paths (propagation direction) diverge slightly due to refraction by the sample as shown in Fig. 3(a). This refraction angle, ds, is given by

$$ds = \frac{\lambda}{2\pi}\frac{d\theta}{dx},\tag{9}$$

where $d\theta/dx$ is the spatial differential of the phase shift. Therefore, phase shift $d\theta$ can be obtained by calculating the integral of ds. The ds can be detected using the X-ray diffraction of the perfect crystal placed downstream of the sample for analyzing. The intensity of the diffracted X-ray changes depending on the incidence angle to the crystal around the Bragg

angle, θ_B, as shown in Fig. 3(b). This curve is called a rocking curve, and its full width at half maximum (FWHM) is a few arc seconds for a perfect silicon crystal. In addition, the slopes near the angles θ_L or θ_H, where the diffracted intensity is half the maximum, are very steep. Therefore, the intensity of the diffracted X-ray can be made almost proportional to *ds* by adjusting the analyzer crystal to θ_L or θ_H. Namely, the crystal functions as an angular analyzer of the *ds*, and the *ds* can be very sensitively detected as changes in the intensity of the diffracted X-ray.
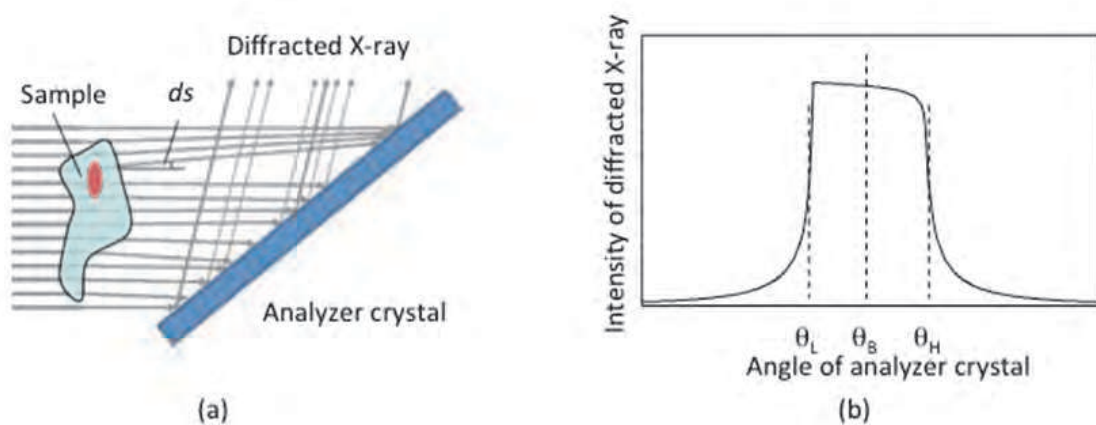
Fig. 3. (a) Diffraction-enhanced method and (b) diffracted X-ray intensity (rocking curve) obtained by rotating analyzer crystal (calculation).

To obtain a correct phase map without the effect of the X-ray absorption by the sample, measurement methods using multiple diffraction images taken at different crystal angles are required. One measurement method is diffraction-enhanced imaging using two (i.e., "T") images (DEIT) (Chapman et al., 1997). The *ds* is calculated as

$$ds(x, z) = \frac{I_H(x,z,)R(\theta_H) - I_L(x,z,)R(\theta_L)}{I_H(x,z,)\left(\frac{dR}{d\theta}\right)(\theta_H) + I_L(x,z,)\left(\frac{dR}{d\theta}\right)(\theta_L)}, \tag{10}$$

where $R(\theta)$ is the reflectivity of the analyzer crystal and *I* is the intensity of the diffracted X-ray. Only two images are needed, so this method is suitable for quick measurements such as *in vivo* observations. However, if the *ds* is larger than the FWHM of the rocking curve, the intensity of the diffracted X-ray shows an incorrect value because the angular point on the rocking curve is far from the peak, where the *ds* is not proportional to the diffracted intensity. Therefore, the dynamic range of density of DEIT is not as wide as that of the method obtained by scanning the analyzer crystal throughout the rocking curve, i.e., diffraction-enhanced imaging using many (i.e., "M") images (DEIM) (Koyama et al., 2004). The *ds* in DEIM is calculated as

$$ds(x, z) = \frac{\sum_{k=1}^{n} \theta_k I_k(x,z)}{\sum_{k=1}^{n} I_k(x,z)}, \tag{11}$$

where θ_k is the angle of the analyzer crystal and I_k is the intensity of the diffracted X-ray at θ_k. The scanning angular range depends on the spatial density changes in the sample. For samples with large spatial density changes, a large range is required to obtain correct images. A long measurement time is required to obtain the images, but the dynamic range is not limited by the angular width of the total reflection of the analyzer crystal.

2.3 Imaging system
2.3.1 Crystal X-ray interferometric imaging (XII) system

A schematic view of an XII system (Yoneyama et al., 2004a; Yoneyama et al., 2005) fitted with a skew-symmetric two-crystal X-ray interferometer (STXI) is shown in Fig. 4. The system consists of an asymmetric crystal, an STXI, positioning tables for the STXI, a sample positioner, and a phase shifter. The imaging system has been set up at beamline BL-14C2 (at the Photon Factory in Tsukuba, Japan) to use the X-ray synchrotron radiation emitted from a vertical wiggler. The X-ray is monochromatized by a Si (220) double-crystal monochromator (not shown), enlarged horizontally by the Si (220) asymmetric crystal, and irradiated onto the first block of the STXI. One interference image generated by the STXI is taken with the charge-coupled device (CCD)-based low-noise X-ray imager for detecting the phase map of the sample. The other image is used in the feedback system stabilizing the X-ray phase fluctuation. The main specifications of the imaging system are shown in Table 1.

To attain subnano-radian mechanical stability of the STXI for fine observation, the positioning tables of the STXI are simplified as much as possible, made robust against vibration, and driven by laminated piezoelectric translator (PZT) actuators. In addition, the drift rotation is suppressed by the feedback system, which controls the PZT's expansion so as to cancel the movement of the X-ray interference pattern caused by the drift rotation between the crystal blocks of the STXI (Yoneyama et al., 2004b). Due to these features, mechanical stability (standard deviation) within 0.04 nrad was achieved, enabling fine observations of biomedical samples to be obtained.
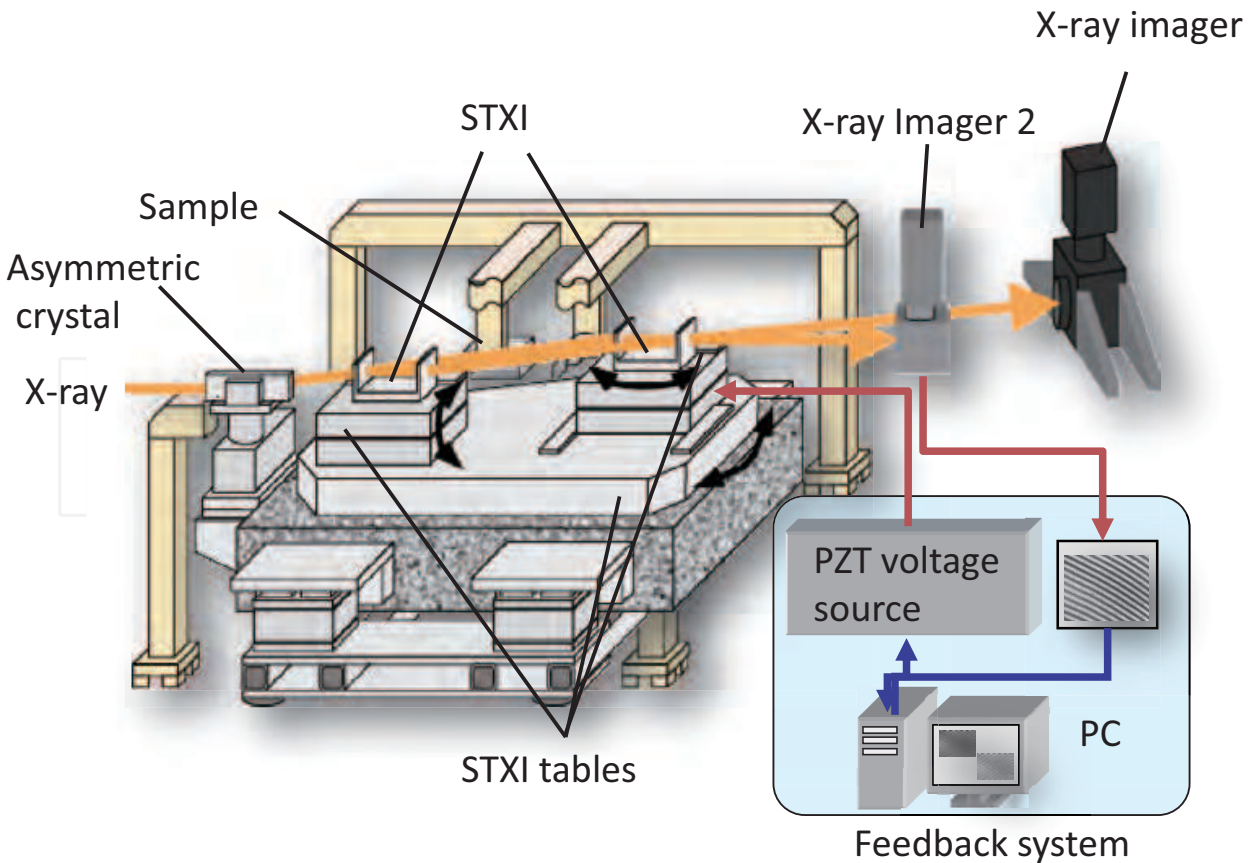

Fig. 4. Schematic view of XII system using two-crystal X-ray interferometer.

X-ray energy	17–52 keV
Field of view	60×30 mm at 17 keV; 25×30 mm at 35 keV
Spatial resolution	Approx. 50 μm
Density resolution	Approx. 1 mg/cm3 for 3D measurement for 2 hours

Table 1. Main specifications of XII system.

The X-ray imager consists of a scintillator that converts X-rays into visible light, a relay-lens system that transfers the light from the scintillator to a camera, and a full-frame-type CCD camera (Momose et al., 2001). The field of view of this imager is 36 × 36 mm, composed of 2048 × 2048 pixels of 18-μm square, and the image-transfer period is about 3 s for a full image. Gd_2O_2S (GOS) was used to fabricate the scintillator. The GOS thickness is 30 μm, and its absorption ratio is 78 and 20% for 17.8- and 35-keV X-rays, respectively. The CCD camera is cooled with water instead of an air fan to avoid any mechanical vibration.

A sample is placed in the object beam path using a sample positioner composed of vertical and horizontal linear tables and a rotational table with the horizontal axis. Each table is driven by stepping motors operated by remote control. A plastic wedge used as a phase-shifter is also positioned by another positioner with the same structure as the sample positioner. Each positioner is attached to rails installed on the frame and can move perpendicular to the interfering beam so that it can be roughly adjusted and the samples can be exchanged. The frame stands independently of the STXI table so as to prevent vibration caused by the motion of the positioner from disturbing the interference.

Interference images for the FS method are taken by scanning the wedge vertically at even intervals. For 3D observation, the sample is rotated perpendicularly to the beam path for 180 degrees by using the rotational table of the sample positioner. The phase-contrast tomograms are obtained as follows.

1. Calculate the phase map from the obtained interference images by the FS method.
2. Unwrap the phase map and then generate a sinogram from it.
3. Calculate the tomograms using a filter-back projection with a Shepp-Logan filter (Shepp & Logan, 1974).

2.3.2 Diffraction-enhanced imaging (DEI) system

A schematic view of a DEI system (Yoneyama et al., 2008) is shown in Fig. 5. The system consists of an asymmetric crystal, an analyzer crystal, and an X-ray imager. The X-ray synchrotron radiation emitted from the storage ring is monochromatized and enlarged horizontally by the Si (220) symmetric crystal in the same way as in the XII system, and it irradiates the sample directly. The X-ray beam that has passed through the sample is diffracted by the Si (220) analyzer crystal placed downstream of the sample and is detected by the same X-ray imager used in the XII system. The main specifications of the DEI system are shown in Table 2.

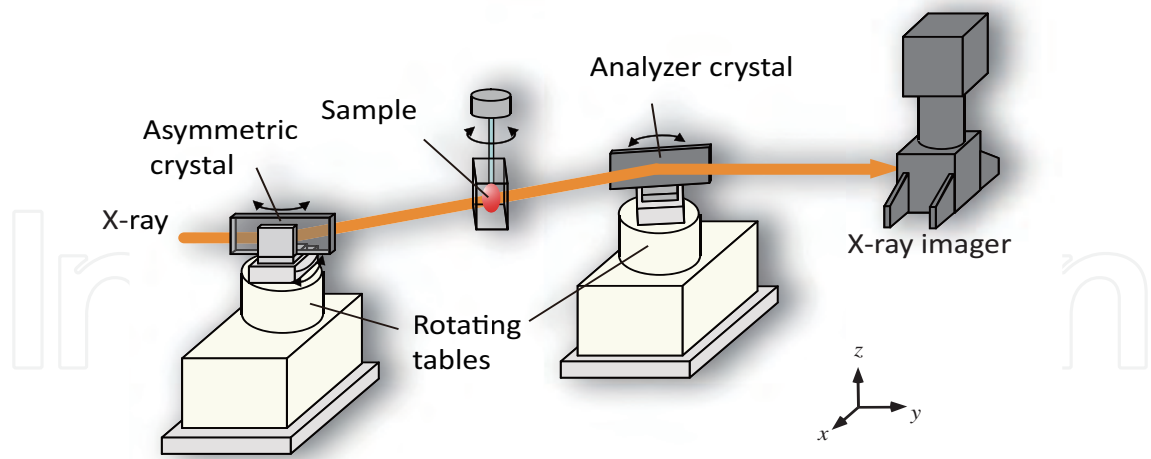| X-ray energy	17–70 keV
Field of view	60×30 mm at 17 keV; 8×30 mm at 70 keV
Spatial resolution	Approx. 50 μm
Density resolution	More than a few mg/cm3 for 3D measurement for 2 hours

Table 2. Main specifications of DEI system.

Fig. 5. Schematic view of DEI system using Si (220) diffraction.

The asymmetric and analyzer crystals are mounted on a precise rotational mechanism consisting of a vertical rotational table and a tilt table. Each table is driven by a stepping motor remotely, and the rotational resolutions are 0.05 and 8 µrad for horizontal and tilt rotation, respectively. By using these precise tables, the drift rotation of the analyzer crystal can be made negligible. The sample is positioned by a sample positioner composed of vertical linear tables and a rotational table with the vertical axis. For 3D observation, the sample is rotated vertically for 180 degrees by using the rotational table. The tomograms are obtained as follows.

1. Calculate the *ds* map from obtained diffracted X-ray images by using equation (10) or (11).
2. Calculate the phase map by using

$$d\theta = \frac{2\pi}{\lambda} \int ds(x,z)\, dx.$$

3. Generate a sinogram from the phase map.
4. Calculate the tomograms using a filter-back projection with a Shepp-Logan filter.

2.4 Comparison of imaging performance

Figure 6 shows the phase maps of a formalin-fixed rat liver obtained using (a) XII, (b) DEIT, (c) DEIM, and (d) conventional radiography (absorption contrast). Each image was 24-mm wide and 25-mm high. The X-ray energy was set to 17.8 keV, and the total X-ray dose for obtaining the images was adjusted to remain at the same level by changing the exposure time. The sample was put in a sample cell filled with formalin to prevent rapid phase shifts caused by a large density difference between the sample and its surrounding environment. The fringe number for FS in XII was set at 3, and 11 diffraction images were used for DEIM. Large blood vessels with a diameter of ~1 mm can be clearly seen in phase maps (a) to (c), but not in (d), because the phase shift of saline solution injected in blood vessels is different from that of the surrounding liver tissues (Takeda et al., 2002). Blood vessels with a diameter of less than 100 µm can be seen in (a), but not in (b) and (c). In addition, phase maps (b) and (c) include many horizontal noise lines caused by the integral calculation of *ds* along the x-axis (horizontal direction in the figures). As shown here, the radiographic image quality of XII is better than that of DEIM and DEIT because DEI has no sensitivity in the vertical direction.
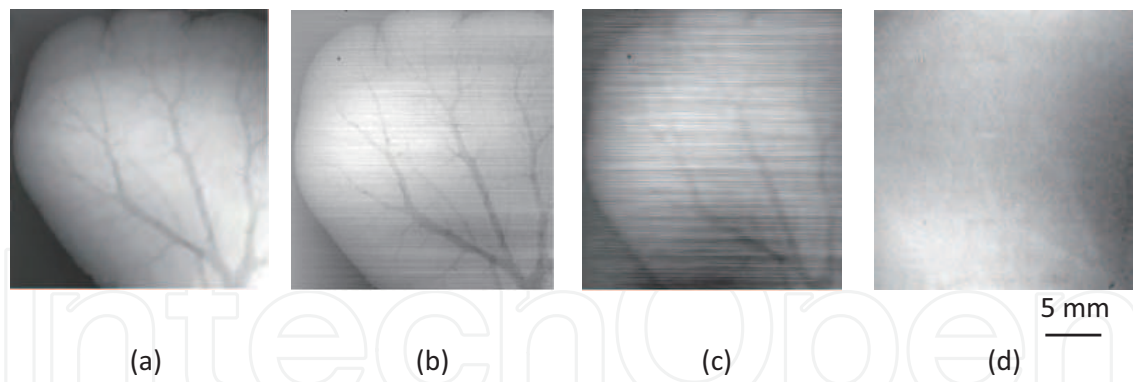
Fig. 6. Phase maps of rat liver obtained using (a) XII, (b) DEIT, (c) DEIM, and (d) conventional radiography. Large blood vessels with a diameter of ~1 mm can be clearly seen in every phase map, but blood vessels with a diameter of less than 100 μm can only be seen in (a).

Figure 7 shows 3D images and tomograms of a formalin-fixed rat kidney obtained using (a) XII, (b) DEIT, and (c) DEIM. The X-ray energy was set at 35 keV, and the X-ray dose was adjusted to remain at the same level in the same way as in radiographic imaging. The sample was rotated in the sample cell filled with formalin to decrease artifacts caused by a large density difference between the sample and its surrounding environment. The image quality of (a) is better than that of (b) and (c); soft tissues such as blood vessels, medullas, and cortexes are clearly visible in (a), while the details of tissues cannot be distinguished in (b) and (c).
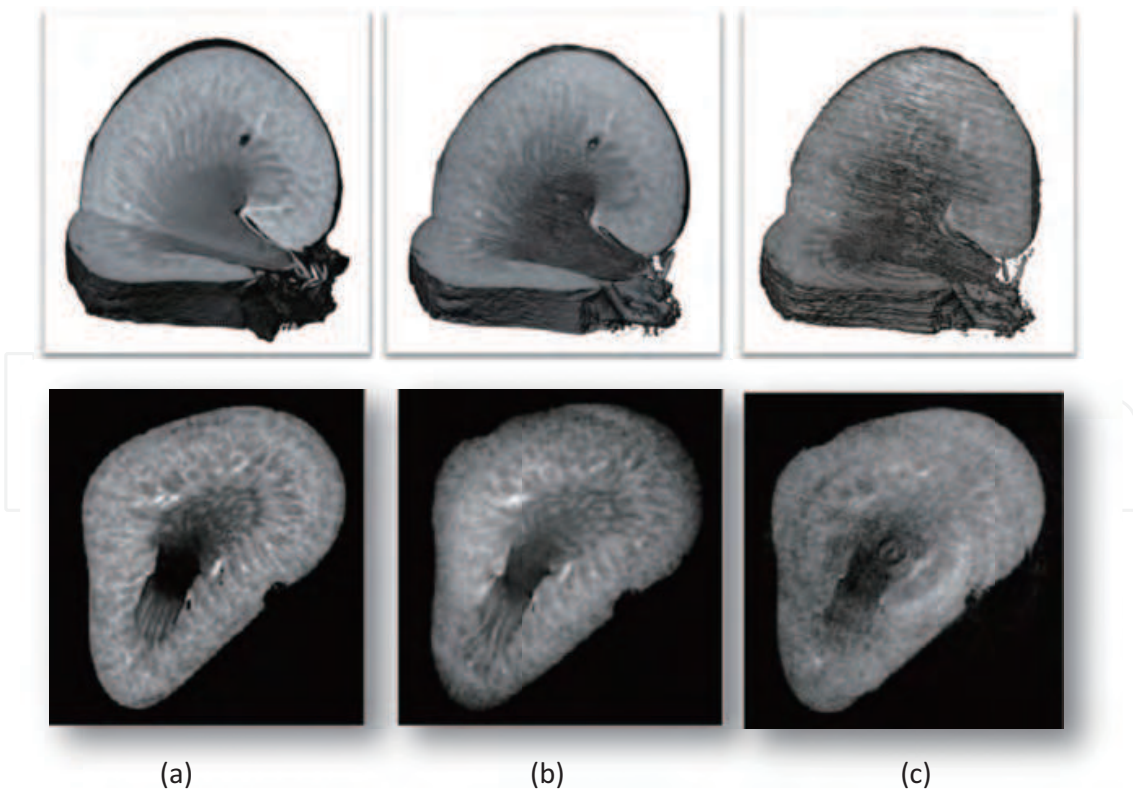
Fig. 7. 3D images and tomograms of rat kidney obtained using (a) XII, (b) DEIT, and (c) DEIM, with 35-keV X-ray beam. Soft tissues such as blood vessels, medullas, and cortexes are clearly visible in (a), while only cortexes can be distinguished in (b) and (c).

The density resolutions of XII, DEIT, and DEIM for X-ray intensities at the sample position are shown in Fig. 8. The density resolutions were calculated from the standard deviation of the relative refractive index in the background regions in each obtained tomogram. The X-ray energy was set at 35 keV, and typical total exposure times to obtain one data set for one projection were 1.5, 3, 7.5, 15, and 30 s. To conduct the comparison correctly, the same phantom consisting of polyethylene tubes filled with saline solution was used with each imaging system. As expected from the observations of the kidney, this result shows that the sensitivity of XII was the highest among these methods. In addition, the sensitivity of DEIM is about one fifth that of DEIT because all the images (including those obtained at the angles far from the Bragg condition) were used to calculate the *ds* for a wider dynamic range of density. Note that images obtained by DEIT and DEIM include many horizontal noise lines as shown in Fig. 6, and therefore it is thought that the relative difference of the density resolution between XII and DEIs is larger in 3D observations.
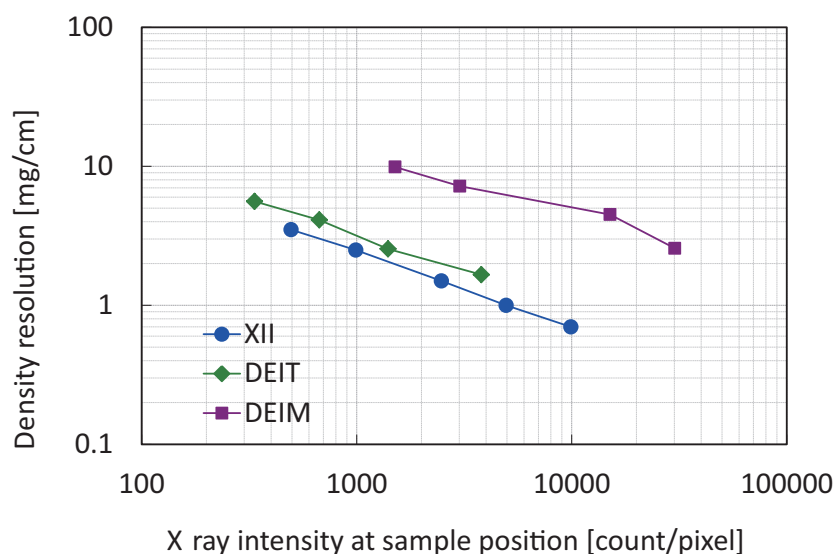

Fig. 8. Density resolution of XII, DEIT, and DEIM at each X-ray intensity.

A 3D image of a formalin-fixed rat tail obtained using DEIM with a 35-keV X-ray beam is shown in Fig. 9. The bone, disc, and hair are clearly visible. The density between the disc and the muscle was very different; therefore, the phase shift caused by the tail was too large and could not be detected correctly using either XII or DEIT. DEIM has lower sensitivity than the other methods, but it has a wide dynamic range of density and enables observation of a sample having regions with large differences in density.

3. Application for observation of pathological samples

Current biomedical research commonly uses various imaging techniques, such as X-ray CT, magnetic resonance imaging (MRI), positron emission tomography (PET), optical imaging, and supersonic imaging, to visualize the inner structures of objects (Wu & Tseng, 2004; Weissleder, 2006; Grenier et al., 2009; Hoffman & Grambhir, 2007). Micro-imaging techniques require high spatial resolution of the micrometer order and high contrast resolution, especially for basic biomedical research with small animals. For example, micro-X-ray CT with a conventional X-ray tube has spatial resolution of a few micrometers, but the contrast resolution is significantly low (Ritman, 2002).
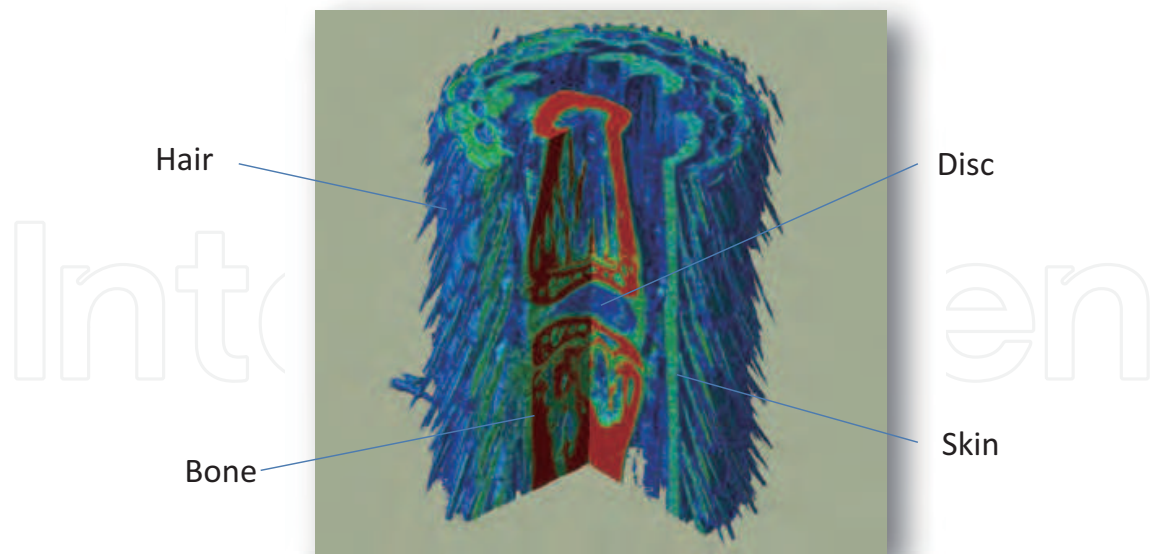
Fig. 9. 3D images of rat tail obtained using DEIM with 35-keV X-ray beam. Bone, disc, and hair are clearly visible.

X-ray interferometric imaging clearly depicts minute density differences within biological objects composed of low atomic number elements. Thus, this imaging technique was applied to observe biomedical objects, and detailed images that cannot be visualized by conventional X-ray imaging techniques was obtained. Here, we describe *ex-vivo* and *in-vivo* biomedical images obtained using XII.

3.1 Breast cancer imaging

A conventional X-ray mammogram is obtained as a projection image, and a lower X-ray energy of 18 keV is used to detect micro-calcification of more than 0.2 mm and soft tissue mass lesions of more than 2–3 mm. The phase-contrast X-ray imaging technique has high sensitivity to detect soft tissue lesions and enables the X-ray exposure for the patient to be decreased. The diagnosis of breast cancer is one of the most important targets of this technique.

An absorption-contrast X-ray image, phase map, and histological picture stained with hematoxylin-eosin of an invasive ductal breast cancer specimen are shown in Fig. 10. Breast tissue and its cancer, which is composed of fat, soft tissue, and micro-calcification, have a wide density difference. Therefore, to increase the dynamic range of density, a high X-ray energy of 51 keV was used in interferometric imaging of breast tissue specimens. In the phase map, the mosaic-like structure of breast cancer is clearly depicted, resembling the histological picture, whereas in the absorption-contrast image, the cancer and surrounding breast soft tissue are shown as homogeneous (Takeda et al., 2004c). The signal to noise ratio of the phase map at 51 keV on soft tissue against surrounding water was approximately 478-folds higher than that of the absorption X-ray image at 17.7 keV.

The phase map at 51 keV also had an excellent ability to enable differentiation of minute changes in the soft tissue density and detection of micro-calcifications of 0.036 mm that were undetected by the absorption-contrast X-ray technique. The phase map of the inner breast cancer structures matched well with pathological pictures. Therefore, XII might detect an

extremely early stage of breast cancer, and thus it could improve the prognosis for the patient. In addition, the use of 51-keV X-ray energy markedly reduces the X-ray exposure of the patient. For example, to image a 50-mm-thick object, a 51-keV X-ray dose by XII would be less than 1/80 of the dose in conventional X-ray mammography.
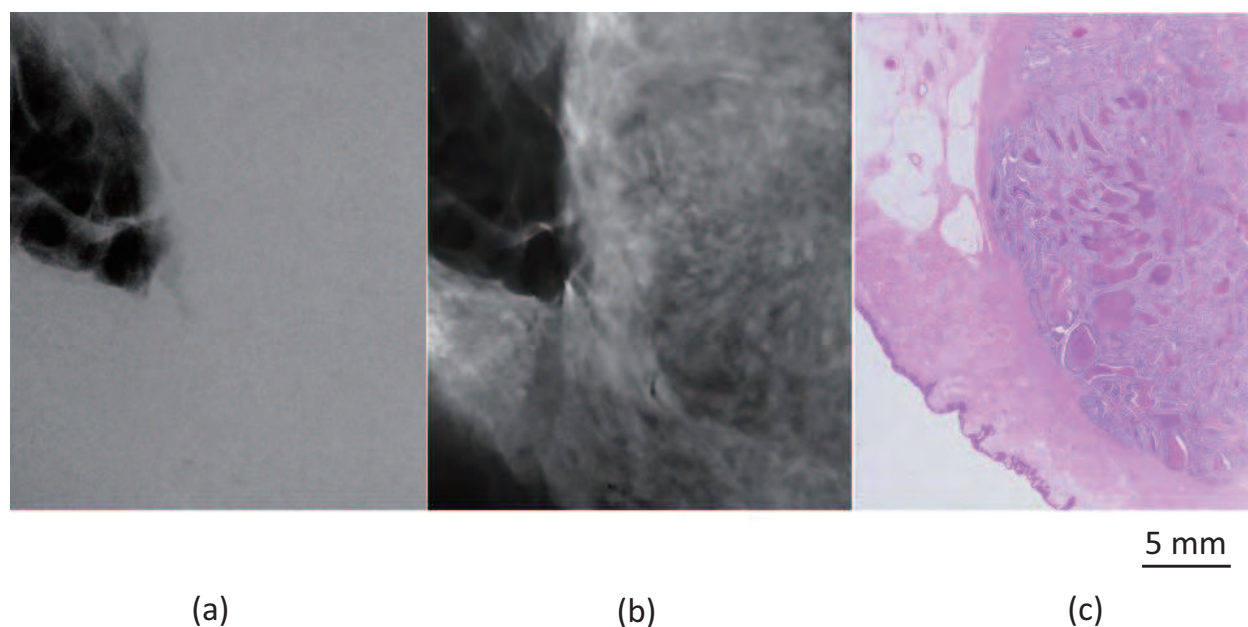

5 mm

(a)   (b)   (c)

Fig. 10. (a) Absorption-contrast image, (b) phase map, and (c) pathological picture of 10-mm-thick formalin-fixed specimen of invasive ductal breast cancer.

3.2 Formalin-fixed colon cancer specimens from nude mice

Imaging of cancer is very important for diagnosis and determining a treatment strategy. In a conventional X-ray CT image, the absorption differences among cancer, fibrosis, necrosis, and normal tissues are difficult to detect because the differences in the linear attenuation coefficients of these tissues are very small. As mentioned earlier, XII enables visualization of the inner structures of human cancer specimens (Takeda et al., 2000) and animal cancer specimens (Momose et al., 1996; Takeda et al., 2004d), the brain (Beckmann et al., 1997), and the kidney (Wu et al., 2009) without contrast agents composed of heavy atomic elements. Here, we describe the images of cancer specimens obtained using XII at 35-keV X-ray energy.

The formalin-fixed specimens, approximately 12 mm in diameter, were of colon cancer that had been implanted in nude mice with a subsequent ethanol injection performed to examine the therapeutic effect of ethanol. Obtained sectional images clearly depicted the detailed inner structures of the subcutaneous implanted colon cancer mass, including cancer lesions, necrosis, mixed changes, surrounding tumor vessels, the subcutaneous thin muscle layer, subcutaneous tissue, and skin (Fig. 11). Cancer cells underwent necrosis in the central portion of the cancer mass due to the ethanol injection. In addition, the bulging of cancer from the thin muscle layer was well demonstrated. The pathological picture well resembled the phase-contrast sectional image. Thus, pathological information generated by the difference in density could be detected clearly. This indicates that quantitative evaluation could be easily performed using XII for new therapeutic applications.
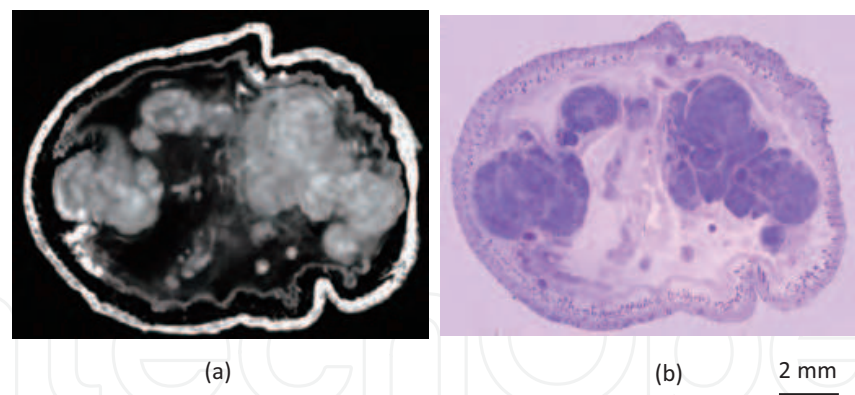
Fig. 11. (a) Phase-contrast X-ray CT and (b) pathological picture of colon cancer implanted in nude mouse.

3.3 Amyloid plaques in mouse model of Alzheimer's disease

Alzheimer's disease (AD) is the most common cause of dementia, and it is pathologically characterized by the deposition of amyloid plaques. Amyloid plaques, composed of densely aggregated β-amyloid (Aβ) peptides, are believed to play a key role in the pathogenesis of AD. Therefore, visualization of amyloid plaques is believed important for diagnosing AD. In this study, the brains from 12 PSAPP mice, an excellent AD model mouse for studying amyloid deposition, were imaged by XII at 17.8 keV X-ray energy.

Numerous bright white spots having high density were typically observed in the brains of 3 PSAPP mice at the age of 12 months, whereas no spots were depicted in an age-matched control mouse without the use of contrast agents. An example is shown in Fig. 12 (Noda-Saita et al., 2006). To confirm the identity of these bright spots, histological studies were performed after the observation. The bright spots were found to be identical to amyloid plaques. Finally, we performed quantitative analysis of Aβ spots in the brains of 3 PSAPP mice each at 4, 6, 9, and 12 months of age. The results showed that the quantity of Aβ spots clearly increased with age as shown in Fig. 13.

(a) Control mouse brain   (b) PSAPP mouse brain
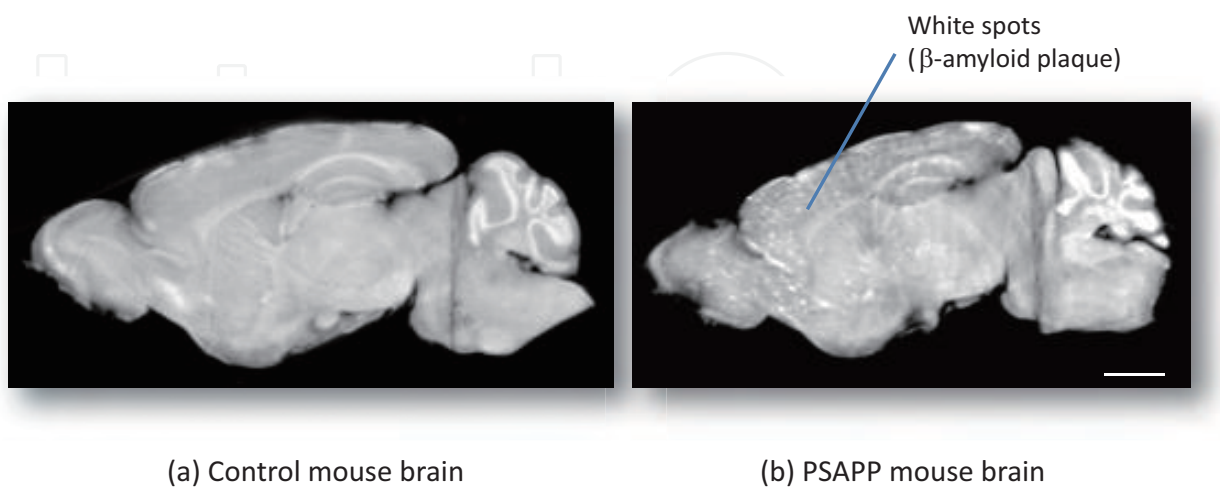
Fig. 12. Amyloid plaque in 12-month old mouse model of Alzheimer's disease. Identification of bright spots observed in brain of PSAPP mouse, but age-matched control mouse did not show such spots. Scale bars = 2 mm.
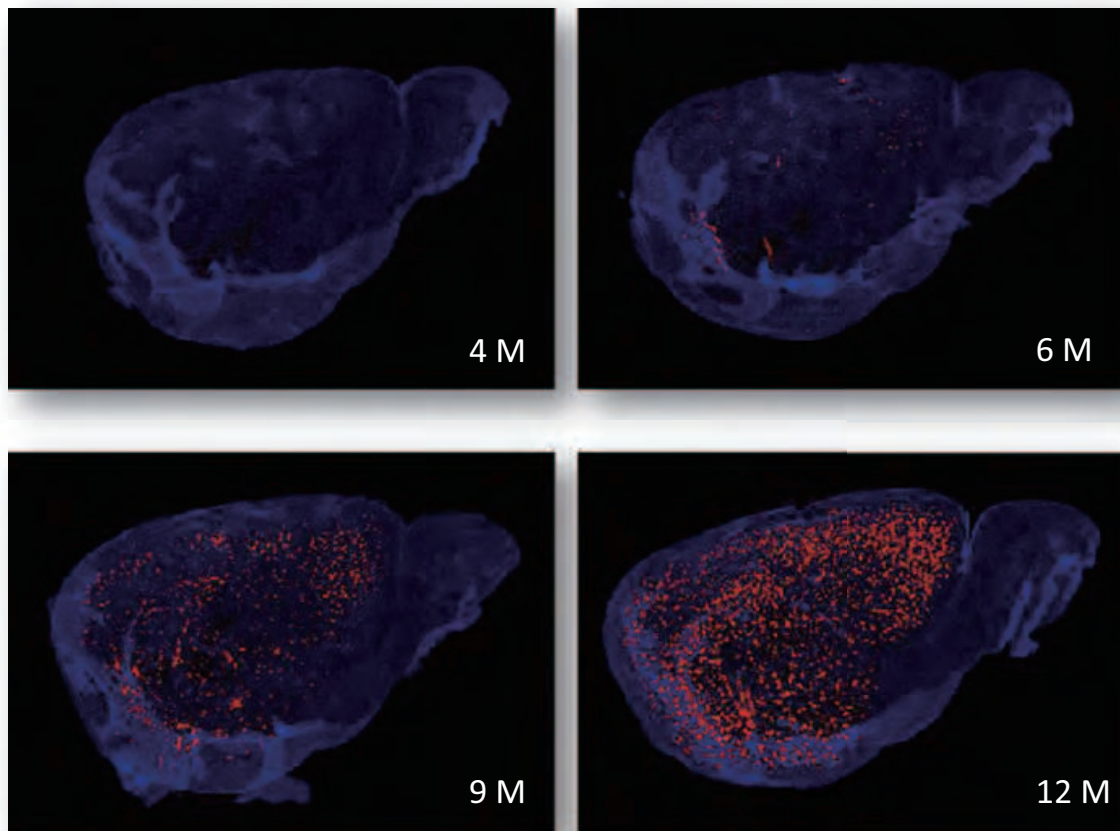
Fig. 13. Representative 3D images of Aβ spots (orange) in brain (cerebral cortex and hippocampus) of PSAPP mice at 4, 6, 9, and 12 months old.

3.4 Phase-contrast X-ray CT imaging of live mouse

In-vivo observation of a small animal disease model is very important for establishing a new diagnostic and/or treatment method in basic clinical research. With the benefit of a two-crystal interferometer, *in-vivo* imaging of a mouse implanted with colon cancer was achieved using the XII system (Takeda et al., 2004). Furthermore, sequential observation was performed to examine the treatment effect of paclitaxel as a cancer drug (Yoneyama et al., 2006).

A series of horizontal slice images obtained from a tumor following injection of paclitaxel is shown in Fig. 13. The tumor size did not change significantly, but the low density area (necrosis) near the center became larger gradually. A typical 3D image observed during the second day after cancer drug therapy started is shown in Fig. 14. The tumor was 10 mm in diameter and ~6 mm thick. The blue area indicates a low-density region and the green area indicates a high-density region.

These results showed that the phase-contrast X-ray CT enables us to perform detailed observation with high spatial resolution without harming the target, and therefore *ex-* and *in-vivo* visualization of biomedical objects is believed very useful for biomedical research.
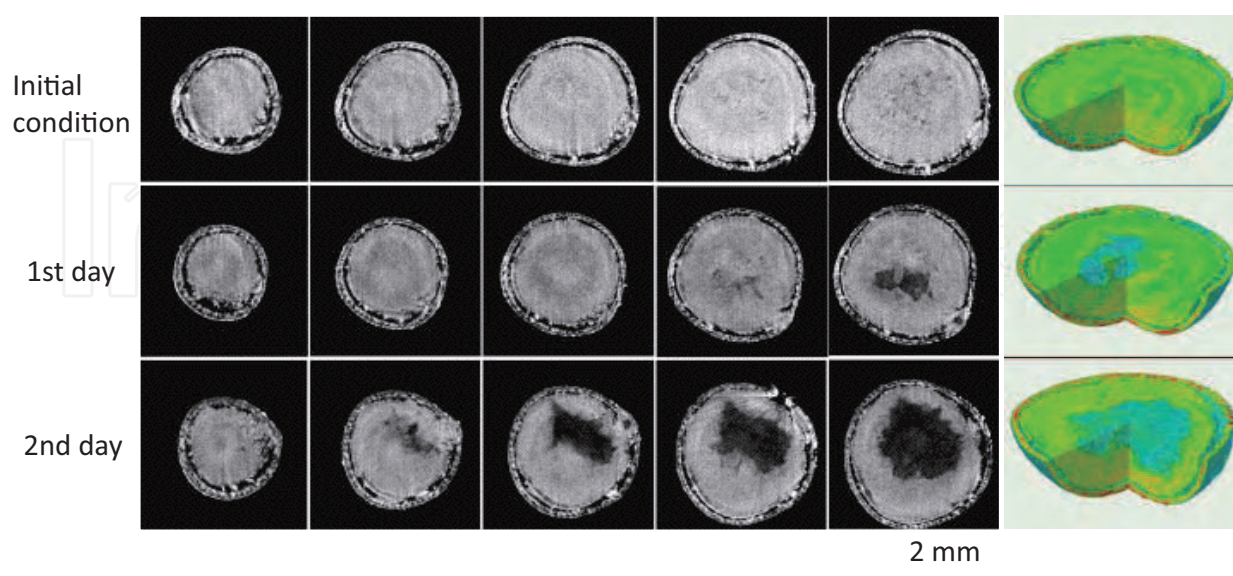
Fig. 14. Series of horizontal slice images of colon cancer and 3D in-vivo phase-contrast X-ray CT images taken before and after anti-cancer drug therapy started.

4. Application for embryo imaging

Embryos undergo complicated morphogenetic changes during the course of development. Classically, drawings and solid reconstruction were used to demonstrate the 3D changes of embryonic structures. The wax plate technique of reconstruction was used for embryology, and based on the reconstructed models, numerous accurate drawings of embryos were produced by hand (see Yamada et al., 2006). During the past 20 years, computer-assisted reconstruction of biological structures has become available, which has enabled the reconstruction of various 3D structures from serial sectional images. Non-destructive imaging technologies such as X-ray CT and magnetic resonance (MR) imaging, which were originally developed as non-invasive diagnostic tools in clinical medicine, have also been applied to the imaging and 3D reconstruction of tiny biological structures such as embryos. The MR microscopic technology has been widely used to scan and visualize relatively small samples, including mammalian embryos (Smith et al., 1996; Smith, 1999; Haishi et al., 2001; Yamada et al., 2010), but MR microscopy does not yield resolution or contrast high enough for millimetre-sized embryos. Conventional X-ray CT was also developed for microscopic observation of small structures, but it is not appropriate for soft tissues such as embryos.

Sequential images during mouse embryo development obtained by the DEI system are shown in Fig. 15. By using formalin-fixed mouse embryos, detailed observation of the internal organs can be made throughout the early to late stages of mouse embryonic development by tomographs, as well as of the external appearance by surface reconstruction. The developing bone structures do not affect the phase-contrast images (see E15.5 and E17.5 in Fig. 15).
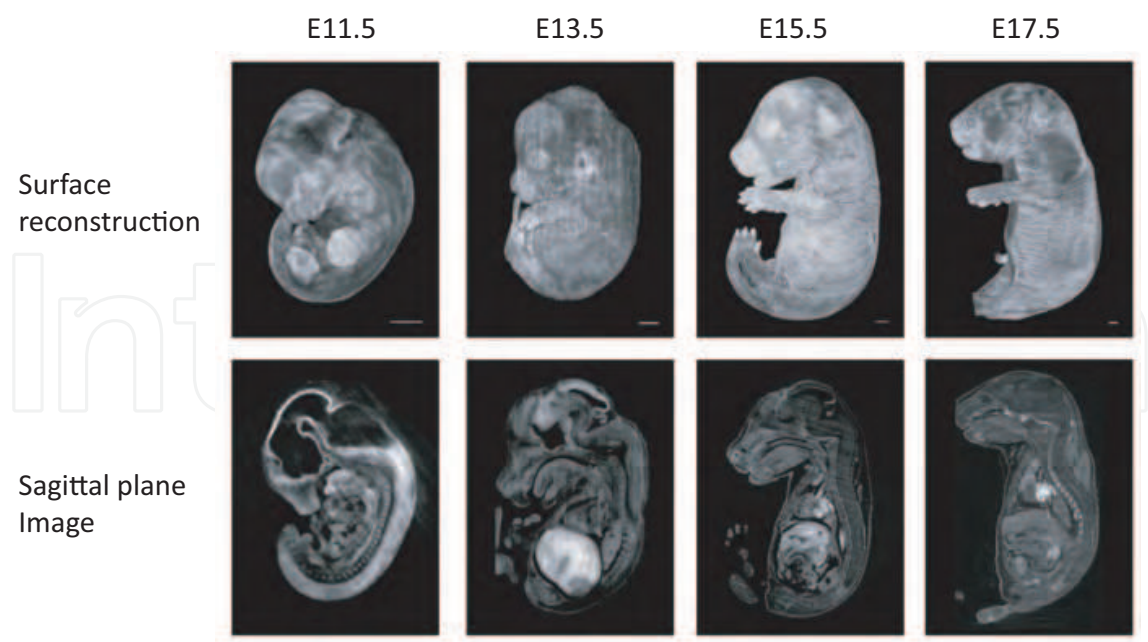
Fig. 15. Sequential images of mouse embryo development. Bars = 1 mm.

Embryo images obtained by the XII and DEI systems are shown in Fig. 16. Both systems can provide fine surface reconstruction and images of the internal structure. Images by the XII system seem to be better than those of the DEI system for the same embryo, although the scan time of DEI (1 hr) is much shorter than that of XII (4–5 hrs). The image sharpness can be affected by the direction of the rotation of the samples. Some precious samples were not glued directly on the stage but were embedded in agar, which was then fixed on the stage by an adhesive agent. Therefore, small deformation of the agar by gravity may affect the images by the XII system.
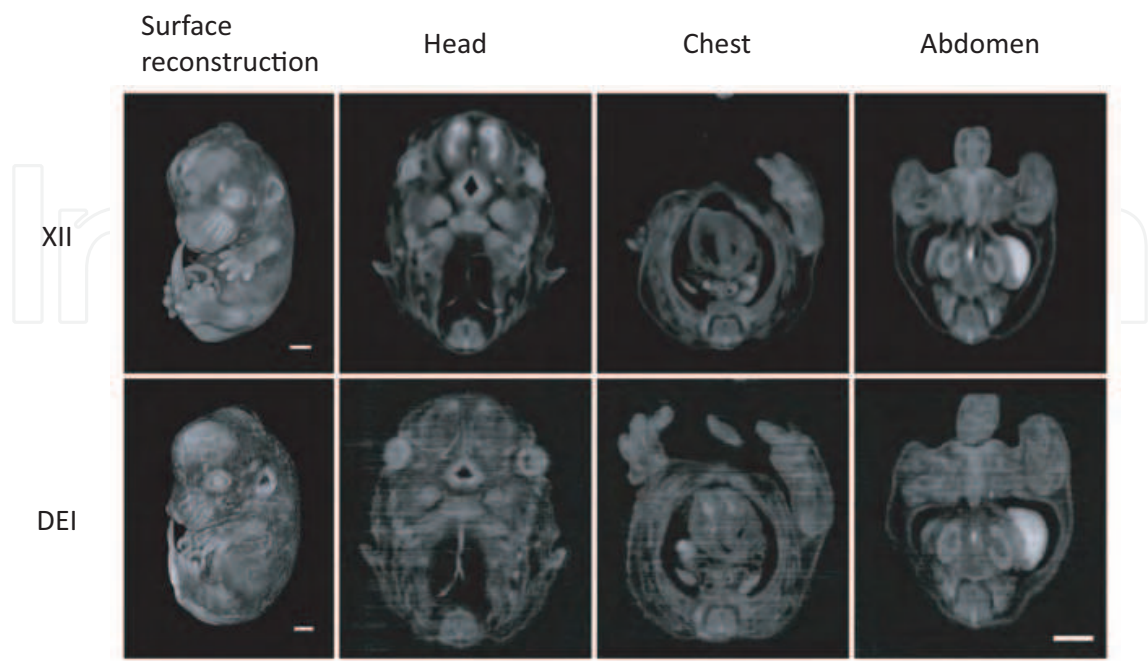
Fig. 16. Images by XII and DEI systems for E13.5 mouse embryo in Fig. 15. Bars = 1mm.

These images show that the phase-contrast X-ray CT has a wide enough field and high enough resolution for observation and analyses of morphological changes during embryo development.

5. Conclusion

Phase-contrast X-ray imaging is a novel imaging method using the X-ray phase shift caused by a sample as image contrast. The sensitivity of the method is much higher than that of the conventional method using X-ray absorption by the sample. To detect X-ray phase shift, many detection methods such as X-ray interferometric imaging (XII) and diffraction-enhanced imaging (DEI) have been developed. XII has the highest sensitivity (density resolution) and therefore is suitable for observations requiring high density resolution, such as visualization of β-amyloid plaques. DEI has a wide dynamic range of density and is thus suitable for observation of samples including regions with large differences in density, such as bone and soft tissues. Many fine observations of pathological soft tissues and mice embryos were performed by selecting the most suitable imaging method. The results show that phase-contrast X-ray imaging enables us to perform fine observation of biomedical and organic samples without extreme X-ray exposure or any supplemental agents.

6. Acknowledgments

7. References

Ando, M., Sugiyama, H., Kunisada, T., Shimao, D., Takeda, K., Hashizume, H., & Inoue, H. (2004). Construction of X-ray dark-field imaging with a view size of 80 mm square and first visualization of human articular cartilage of femoral head under a nearly clinical condition. *Jpn. J. Appl. Phys.*, 43, L1175-L1177

Becker, B. P. & Bonse, U. (1974). The skew-symmetric two-crystal X-ray interferometer. *J Appl. Cryst.*, 7, 593–598.

Beckmann, F., Bonse, U., Busch, F., & Gunnewig, O. (1997). X-ray microtomography using phase contrast for the investigation of organic matter. *J. Comput. Assist. Tomogr.*, 21, 539–553.

Bonse, U. & Hart, M. (1965). An X-ray interferometer. *Appl. Phys. Lett.*, 6, 155–156.

Bruning, J. H., Herriott, D. R., Gallagher, J. E., Rosenfeld, D. P., White, A. D., & Brangaccio, D. J. (1974). Digital wavefront measuring interferometer for testing optical surfaces and lenses. *Appl. Opt.*, 13, 2693–2703.

Chapman, D., Thomlinson, W., Johnston, R. E., Washburn, D., Pisano, E., Gmur, N., Zhong, Z., Menk, R., Arfelli, F., & Sayers, D. (1997). Diffraction enhanced x-ray imaging. *Phys. Med. Biol.,* 42, 2015–2025.

Connor, M. D., Benveniste, H., Dilmanian, F. A., Kritzer, M. F., Miller M. L., & Zhong, Z. (2009). Computed tomography of amyloid plaques in a mouse model of Alzheimer's disease using diffraction enhanced imaging. *Neuroimage,* 46, 908–914.

Davis, T. J., Gao, D., Gureyev, T. E., Stevenson, A. W., & Wilkins, S. W. (1995). Phase contrast imaging of weakly absorbing materials using hard X-rays. *Nature,* 373, 595–598.

Donath, T., Pfeiffer, F., Bunk O., Grünzweig, C., Hempel, E., Popescu, S., Vock, P., & David, C. (2010). Toward clinical X-ray phase-contrast CT: Demonstration of enhanced soft-tissue contrast in human specimen, *Investigative Radiology,* 45, 445–452.

Grenier, N., Sardanelli, F., Becker, C. D., Walecki, J., Sebag, G., Lomas, D. J., & Krestin, J. P. (2009). Development of molecular imaging in the European radiological community, *European Radiology,* 13, 655–656.

Haishi, T., Uematsu, T., Matsuda, Y., & Kose, K. (2001). Development of a 1.0 T MR microscope using a Nd-Fe-B permanent magnet. *Magn. Reson. Imaging,* 19, 875–880.

Hoffman, J. M. & Gambhir, S. S. (2007). Molecular imaging: the vision and opportunity for radiology in the future. *Radiology,* 244, 39–47.

Ingal, V. N. & Beliaevskaya, E. A. (1995). X-ray plane-wave topography observation of the phase contrast from a non-crystalline object. *J. of Physics* D, 28, 2314–2317.

Koyama, I., Hamaishi, Y., & Momose, A. (2004). Phase tomography using diffraction enhanced imaging. *AIP Conference Proceedings,* 705, 1283–1286.

Mollenhauer, J., Aurich, M. E., Zhong, Z., Muehleman, C., Cole, A. A., Hasnah, M., Oltulu, O., Kuettner, K. E., Margulis, A., & Chapman, L. D. (2002). Diffraction-enhanced X-ray imaging of articular cartilage. *Osteoarthritis and Cartilage,* 10, 163–171.

Momose, A. & Fukuda, J. (1995). Phase-contrast radiographs of nonstained rat cerebellar specimen. *Med. Phys.,* 22, 4, 375–380.

Momose, A. (1995). Demonstration of phase-contrast x-ray computed tomography using x-ray interferometer. *Nucl. Inst. and Meth. in Phys. Research* A, 352, 622–628.

Momose, A., Takeda, T., Itai, Y., & Hirano, K. (1996). Phase-contrast x-ray computed tomography for observing biological soft tissue. *Nature Med.,* 2, 473–47.

Momose, A., Takeda, T., Yoneyama, A., Koyama, I., & Itai, Y. (2001). Wide-area phase-contrast X-ray imaging using large X-ray interferometers. *Nucl. Instrum. Meth.,* A467-468, 917–920.

Momose, A., Kawamoto, S., Koyama, I., Hamaishi, Y., Takai, K., & Suzuki, Y. (2003). Demonstration of X-ray Talbot interferometry. *Jpn. J. Appl. Phys.,* 42, L866-L868.

Momose, A., Yashiro, W., & Kuwarara, H. (2009). Grating-based X-ray phase imaging using multiline X-ray source. *Jpn J. of Appl. Phys.,* 48, 076512.

Noda-Saita, K., Yoneyama, A., Shitaka, Y., Hirai, Y., Terai, K., Wu, J., Takeda, T., Hyodo, K., Osakabe, N., Yamaguchi, T., & Okada M. (2006). Quantitative analysis of amyloid plaques in a mouse model of Alzheimer's disease by phase-contrast X-ray computed tomography. *Neuroscience,* 138, 1205–1213.

Oltulu, O., Zhong, Z., Hasnah, M., Wernick, N. M., & Chapman, D. (2003). Extraction of extinction, refraction and absorption properties in diffraction enhanced imaging. *Journal of Physics* D, 35, 2152–2156.

Pisano, E. D., Johnston, R. E., Chapman, D., Geradts, J., Iacocca, M. V., Livasy, C. A., Washburn, D. B., Sayers, D. E., Zhong, Z., Kiss, M. Z., & Thomlinson, W. C. (2000). Human breast cancer specimens: Diffraction-enhanced imaging with histological correlation-improved conspicuity of lesion detail compared with digital radiography. *Radiology,* 214, 895–901.

Rigon, L., Arfelli, F., & Menk, R. H. (2007). Three-image diffraction enhanced imaging algorithm to extract absorption, refraction, and ultra small-angle scattering, *Appl. Phys. Lett.,* 90, 11, 114102.

Ritman E. L. (2002). Molecular imaging in small animals—roles for micro-CT. *Journal Cellular Biochemistry Supplement,* 39, 116–124.

Smith, B. R., Linney, E., Huff, D. S., & Johnson, G. A. (1996). Magnetic resonance microscopy of embryos. *Comput. Med Imaging Graph,* 20, 483–490.

Smith, B. R., Huff, D. S., & Johnson, G. A. (1999). Magnetic resonance imaging of embryos: an Internet resource for the study of embryonic development. *Comput. Med Imaging Graph,* 23, 33–40.

Snigirev, A., Snigirev, I., Kohn, V., Kuznetsov, S., & Schelokov, I. (1995). On the possibilities of x-ray phase contrast microimaging by coherent high-energy synchrotron radiation. *Rev. Sci. Instrum.,* 66, 5486–5492.

Sunaguchi, N., Yuasa, T., Huo, Q., Ichihara, S., & Ando, M., (2010). X-ray refraction-contrast computed tomography images using dark-field imaging optics. *Appl. Phys. Lett.,* 97, 15, 153701.

Takeda, M., Ina, H., & Kobayashi, S. (1982). Fourier-transform method of fringe pattern analysis for computer-based topography and interferometry. *J. Opt. Soc. Am.,* 72, 156–160.

Takeda, T., Momose, A., Itai, Y., Wu, J., & Hirano, K. (1995). Phase-contrast imaging with synchrotron X-rays for detecting cancer lesions. *Acad. Radiol.,* 2, 799–803.

Takeda, T., Momose, A., Hirano, K., Haraoka, S., Watanabe, T., & Itai, Y. (2000). Human carcinoma: Early experience with phase-contrast X-ray CT image with synchrotron radiation: Comparative specimen study with optical microscopy. *Radiology,* 214, 298–301.

Takeda, T., Momose, A., Wu, J., Yu, Q., Zeniya, T., Lwin, T. T., Yoneyama, A., & Itai, Y. (2002). Vessel imaging by interferometric phase-contrast x-ray technique. *Circulation*, 105, 1708–1712.

Takeda, T., Wu, J., Tsuchiya, Y., Lwin, T. T., Yoneyama, A., Itai, Y., & Itai, Y. (2004a). Vessel imaging by interferometric phase-contrast x-ray technique. *Proc. of 3rd Congress on Heart Disease*, 105, 143–146.

Takeda, T., Yoneyama, A., Wu, J., Lwin, T. T., Tsuchiya, Y., & Hyodo, K. (2004b). In-vivo imaging of cancer implanted in nude mice by two-crystal interferometer-based phase-contrast X-ray CT. *Jpn. J. Appl. Phys.*, 43, L1144-1146.

Takeda, T., Wu, J., Tsuchiya, Y., Yoneyama, A., Lwin, T. T., Aiyoshi, Y., Zeniya, T., Hyodo, K., & Ueno, E. (2004c). Interferometric X-ray imaging of breast cancer specimens at 51 keV X-ray energy. *Jpn. J. Appl. Phys.*, 43, 5652–5656.

Takeda, T., Wu, J., Tsuchiya, Y., Yoneyama, A., Lwin, T. T., Hyodo, K., & Itai, Y. (2004d). Interferometric phase-contrast X-ray CT image of VX2 rabbit cancer at 35 keV X-ray energy. *AIP Conference Proceedings*, 705, 1328–1331.

Weissleder, R. (2006). Molecular imaging in cancer. *Science*, 312, 1168–71.

Weitkamp, T., Diaz, A., & David, C. (2005). X-ray phase imaging with a grating interferometer. *Optics Express*, 13, 6296–6304.

Wernick, M. N., Wirjadi, O., Chapman, D., Zhong, Z., Galatsanos, N. P., Yang, Y., Brankov, J. G., Oltulu, O., Anastasio, M. A., & Muehleman, C. (2003). Multiple-image radiography. *Phys. Med. Biol.*, 48, 23, 3875–3895.

Wilkins, S. W., Gureyev, T. E., Gao, D., Pogany, A., & Steven, A. W. (1996). Phase-contrast imaging using polychromatic hard X-rays. *Nature*, 384, 335–338.

Wu, J. C., Tseng, J. R., & Gambhir, S. S. (2004). Molecular imaging of cardiovascular gene products. *J. Nucl. Cardiol.*, 11, 491–505.

Wu, J., Takeda, T., Lwin, T. T., Momose, A., Sunaguchi, N., Fukami, T., Yuasa, T., & Akatsuka, T. (2009). Imaging renal structures by X-ray phase-contrast microtomography. *Kidney International*, 75, 945–951.

Yamada, S., Uwabe, C., Nakatsu-Komatsu, T., Minekura, Y., Iwakura, M., Motoki, T., Nishimiya, K., Iiyama, M., Kakusho, K., Minoh, M., Mizuta, S., Matsuda, T., Matsuda, Y., Haishi, T., Kose, K., Fujii, S., & Shiota, K. (2006). Graphic and movie illustrations of human prenatal development and their application to embryological education based on the human embryo specimens in the Kyoto collection. *Dev. Dyn.*, 235, 468–477.

Yamada, S., Samtani, R. R., Lee, E. S., Lockett, E., Uwabe, C., Shiota, K., Anderson, S. A., & Lo, C. W. (2010). Developmental atlas of the early first trimester human embryo. *Dev. Dyn.*, 239, 1585–1595.

Yoneyama, A., Momose, A., Seya, E., Hirano, K., Takeda, T., & Itai, Y. (1999). Operation of a separated-type X-ray interferometer for phase-contrast X-ray imaging. *Review of Scientific Instruments*, 70, 4582–4586.

Yoneyama, A., Momose, A., Koyama, I., Seya, E., Takeda, T., Itai, Y., Hirano, K., & Hyodo, K. (2002). Large-area phase-contrast X-ray imaging using a two-crystal X-ray interferometer. *Journal of Synchrotron Radiation*, 9, 277–281.

Yoneyama, A., Takeda, T., Tsuchiya, Y., Wu, J., Lwin, T. T., Koizumi, A., Hyodo, K., & Itai, Y. (2004a). A phase-contrast X-ray imaging system—with a 60×30 mm field of view—based on a skew-symmetric two-crystal X-ray inteferometer. *Nucl. Inst. and Meth. in Phys. Research* A, 523, 217–222.

Yoneyama, A., Takeda, T., Tsuchiya, Y., Wu, J., Lwin, T. T., & Hyodo, K. (2004b). Large-area phase-contrast X-ray imaging system using a two-crystal X-ray interferometer—development of an interference-pattern-based feedback positioning system. *AIP Conference Proceedings*, 705, 1299–1302.

Yoneyama, A., Takeda, T., Tsuchiya, Y., Wu, J., Lwin, T. T., Hyodo, K., & Hirai, Y. (2005). High-energy phase-contrast X-ray imaging using a two-crystal X-ray interferometer. *J. Synchrotron Rad.*, 12, 534–536.

Yoneyama, A., Amino, N., Mori, M., Kudoh, M., Takeda, T., Hyodo, K., & Hirai, Y. (2006). Non-invasive and time-resolved observation of tumors implanted in living mice by using phase-contrast X-ray computed tomography. *Jpn. J. Appl. Phys.*, 45, 1864–1868.

Yoneyama, A., Wu, J., Hyodo, K., & Takeda, T. (2008). Quantitative comparison of imaging performance of X-ray interferometric imaging and diffraction enhanced imaging. *Med. Phys.*, 35, 4724–4734.

Yoneyama, A., Takeda, T., Yamazaki, T., Hyodo, K., & Ueda, K. (2010). High-energy diffraction-enhanced X-ray imaging, *AIP Conference Proceedings*, 1234, 477–480.

Advanced Biomedical Engineering

Edited by Dr. Gaetano Gargiulo

This book presents a collection of recent and extended academic works in selected topics of biomedical signal processing, bio-imaging and biomedical ethics and legislation. This wide range of topics provide a valuable update to researchers in the multidisciplinary area of biomedical engineering and an interesting introduction for engineers new to the area. The techniques covered include modelling, experimentation and discussion with the application areas ranging from acoustics to oncology, health education and cardiovascular disease.

How to reference

In order to correctly reference this scholarly work, feel free to copy and paste the following:

Akio Yoneyama, Shigehito Yamada and Tohoru Takeda (2011). Fine Biomedical Imaging Using X-Ray Phase-Sensitive Technique, Advanced Biomedical Engineering, Dr. Gaetano Gargiulo (Ed.), ISBN: 978-953-307-555-6, InTech, Available from: http://www.intechopen.com/books/advanced-biomedical-engineering/fine-biomedical-imaging-using-x-ray-phase-sensitive-technique

INTECH

open science | open minds